

## Article

# Origin of the Yinshan Pb-Zn-Ag Deposit in the Edong District Section of the Middle–Lower Yangtze River Metallogenic Belt: Insights from In-Situ Sulfur Isotopes

Dengfei Duan, Haobo Jia and Yue Wu \*

Hubei Key Laboratory of Petroleum Geochemistry and Environment, Yangtze University, Wuhan 430100, China; cugddf@163.com (D.D.); 13474290126@163.com (H.J.)

\* Correspondence: leadzinc@163.com

**Abstract:** The investigation into the enigmatic origin of Pb-Zn mineralization within the Middle-Lower Yangtze River Metallogenic Belt has long been marred by a paucity of prior studies. Seeking to alleviate this dearth of knowledge, our study meticulously scrutinizes the Yinshan Pb-Zn-Ag deposit nestled within the Edong district of the belt, endeavoring to cast an illuminating spotlight upon its enigmatic genesis. We identify two distinct epochs: (1) the pre-mineralization pyrite epoch (Epoch I) mainly characterized by colloform and massive pyrite, and (2) the hydrothermal mineralization epoch (Epoch II) which can be further divided into three stages: pyrite-arsenopyrite (stage 1), galena-sphalerite (stage 2), and vein pyrite (stage 3). We conduct in-situ sulfur isotope analyses on sulfide minerals from both epochs, revealing  $\delta^{34}\text{S}$  values ranging from  $-0.5$  to  $4.8\%$  for Epoch I and varying from  $2.2$ – $4.9\%$  (stage 1),  $1.1$ – $3.0\%$ ,  $4.2$ – $7.1\%$  (stage 2), and  $2.1$ – $3.8\%$  (stage 3) for Epoch II. Integrating our sulfur isotope data with the geological characteristics of the deposit, we infer that Pb-Zn mineralization was related to a granite of  $\sim 130$  Ma age. Additionally, our study suggests the possibility of coexisting Mo mineralization beneath the Pb-Zn mineralization. Our findings contribute to a better understanding of the origin of Pb-Zn mineralization in the Middle-Lower Yangtze River Metallogenic Belt.



**Citation:** Duan, D.; Jia, H.; Wu, Y. Origin of the Yinshan Pb-Zn-Ag Deposit in the Edong District Section of the Middle–Lower Yangtze River Metallogenic Belt: Insights from In-Situ Sulfur Isotopes. *Minerals* **2023**, *13*, 810. <https://doi.org/10.3390/min13060810>

Academic Editor: Maria Boni

Received: 17 April 2023

Revised: 4 June 2023

Accepted: 7 June 2023

Published: 14 June 2023



**Copyright:** © 2023 by the authors. Licensee MDPI, Basel, Switzerland. This article is an open access article distributed under the terms and conditions of the Creative Commons Attribution (CC BY) license (<https://creativecommons.org/licenses/by/4.0/>).

**Keywords:** Yinshan deposit; Edong district; in-situ sulfur isotope; Pb-Zn mineralization

## 1. Introduction

The Middle–Lower Yangtze River Valley metallogenic belt (MYRB) resides along the northern margin of the Yangtze craton, renowned for its porphyry–skarn–stratabound Cu–Au–Mo–Fe deposits in uplift areas and magnetite–apatite deposits within Cretaceous fault basins [1]. Despite some investigations into Pb-Zn mineralization within the region, it has received comparably less attention than Cu-Fe deposits [2–8]. Typically, Pb-Zn mineralization in skarn systems is observed at a distance from associated igneous rocks, with limited skarn minerals present due to the requisite lower temperatures for Pb-Zn sulfide mineral deposition [9]. Consequently, the occurrence of Pb-Zn mineralization serves as a valuable indicator for identifying deep-seated magmatic fluid mineralization [9]. Thus, comprehending the genesis of Pb-Zn mineralization assumes paramount importance in the pursuit of exploring Cu-Fe-Au-Mo deposits in the MYRB. Nonetheless, the origin of Pb-Zn deposits in the MYRB remains an issue subject to contention, with varying hypotheses proposed, including: (1) magmatic origin [2–5,7,8,10–20]; (2) Hercynian sedimentary sulfide minerals overprinted by Yanshanian magmatic hydrothermal fluid [21–25]; (3) basinal fluid origin [6]; or (4) organic fluid origin [26,27]. This state of uncertainty has hindered the exploration of Pb-Zn and other metals within the MYRB.

This study focuses specifically on the Yinshan Pb-Zn-Ag deposit, located within the westernmost Edong district of the MYRB. Previous investigations have posited diverse models, such as the sedimentary-exhalative (SedEx) model and sedimentary-reworked

model [28], as well as the epithermal model [10]. Through our examination of the Yinshan deposit, our objective is twofold: to enhance our understanding of its origin and to illuminate the genesis of Pb-Zn deposits within the broader MYRB. We do so by leveraging the potency of in-situ sulfur isotope analysis, a formidable tool for revealing the evolution of sulfur isotopes with high spatial resolution. Due to its small analysis size of 33  $\mu\text{m}$ , this technique is capable of avoiding mixing compositions and providing detailed insights into the sulfur isotopic signatures of individual mineral phases [29]. We employ this technique in conjunction with geological evidence. In doing so, we unveil the magmatic origin of the Yinshan deposit, with some contribution from Hercynian sulfide minerals, albeit without exerting control over the system. Furthermore, our study advances the notion of potential Mo mineralization beneath the Pb-Zn mineralization, thereby underscoring the prospects for further exploration in this region.

## 2. Regional and Deposit Geology

The Yangtze Craton represents a distinct geological entity that exhibits notable distinctions from both the North China Craton and the Cathaysian block. It is spatially separated from these regions by the Dabie Ultrahigh Pressure (UHP) metamorphic belt to the north and a Neoproterozoic suture to the south [30]. Within the eastern part of the Yangtze Craton, three prominent faults traverse the landscape: the Xiangfan-Guangji fault (XGF) to the northwest, the Tangcheng-Lujiang regional strike-slip fault (TLF) to the northeast, and the Yangxin-Changzhou fault (YCF) to the south (Figure 1a). The Middle and Lower Yangtze River metallogenic belt, positioned between the North China Craton and the Yangtze Craton, encompasses various districts, including the Edong, Jiurui, Anqing, Luzong, Tongling, Ningwu, and Ningzhen districts, from west to east (Figure 1a). We specifically focus on the Edong district, which is demarcated by three major fault systems: the Tan-Lu, Xiangfan-Guangji, and Ma-Tuan faults (Figure 1b).

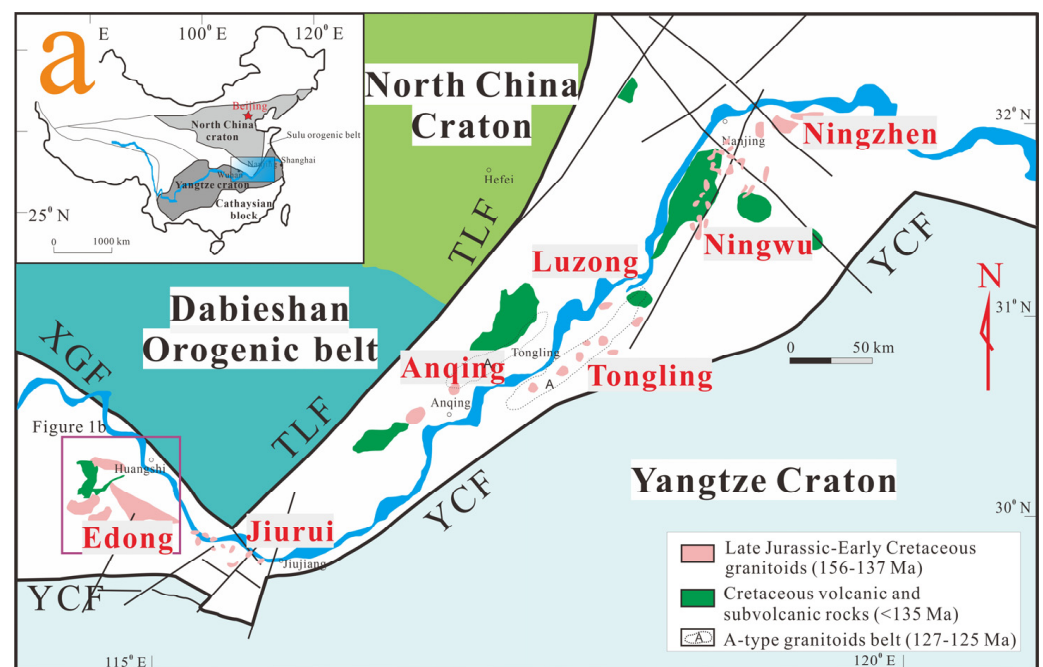
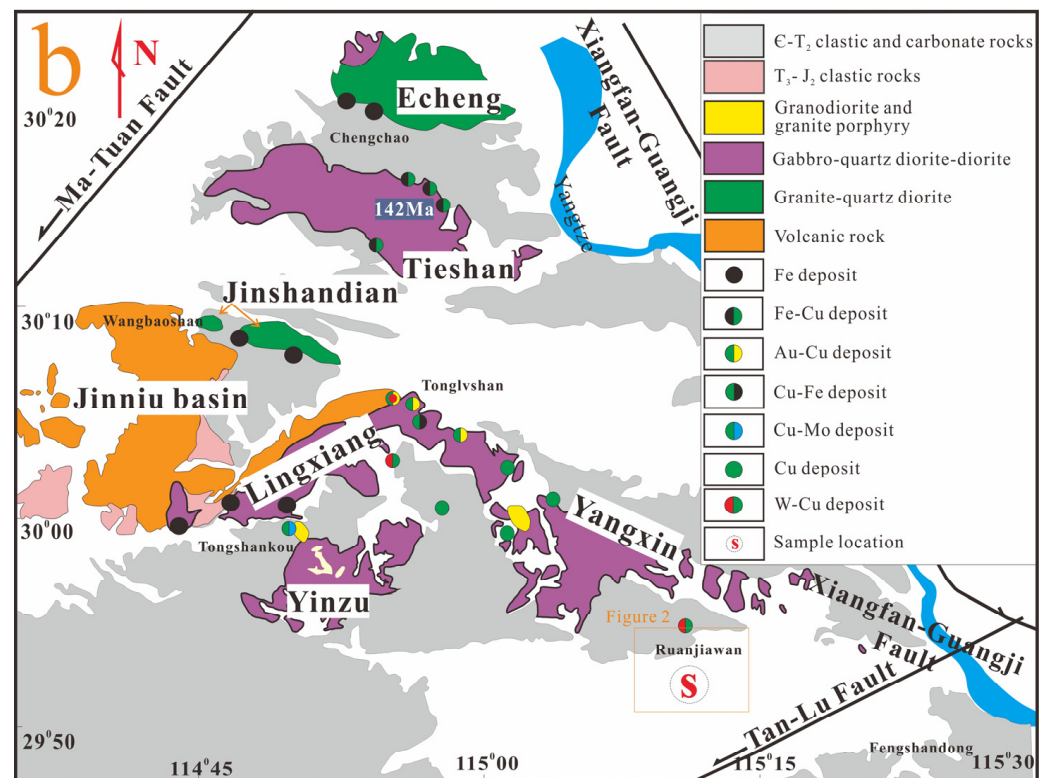


Figure 1. Cont.



**Figure 1.** (a) Schematic illustration of the seven magmatic and metallogenic districts of the Middle and Lower Yangtze River metallogenic belt in the northeastern Yangtze Craton; (b) Granitoid batholiths in the Edong district. TLF-Tangcheng-Lujiang fault, XGF-Xiangfan-Guangji fault, YCF-Yangxin-Changzhou fault. Modified from Xie et al. (2011) [31].

Within the Edong district, the stratigraphic sequence primarily comprises a substantial accumulation of marine sedimentary rocks ranging from the Ordovician to the middle Triassic and exhibiting a thickness exceeding 10 km. Subsequently, continental deposits and Cretaceous volcanic assemblages, spanning the late Triassic to the Cenozoic period, follow this sequence (Figure 1b) [30,32]. The collision between the Yangtze and North China cratons during the middle Triassic period resulted in the folding of pre-Triassic strata within the Edong district [33]. Magmatic events within the Edong district can be classified into two distinct stages. The initial plutonic stage, occurring between 157–132 million years ago (Ma), emplaced the Echeng, Tieshan, Jinshandian, Lingxiang, Yinzu and Yangxin batholiths, alongside numerous smaller intrusions (Figure 1b) [34,35]. It is worth noting that the plutonic rocks can be classified into two categories: one exhibiting elevated Sr/Y and La/Yb ratios, devoid of significant Eu anomalies predating 136 Ma, and the other characterized by diminished Sr/Y and La/Yb ratios, accompanied by a conspicuously negative Eu anomaly ranging from 133 to 127 Ma [36]. The former category is thought to be associated with Cu-Fe mineralization, while the latter is related to Fe mineralization with a more substantial contribution of crust materials [37]. During the subsequent volcanic stage, which erupted between 130–125 Ma [31], over 2 km of volcanic and related sedimentary rocks were deposited, including the Majiashan Formation, the Lingxiang Formation, and the Dasi Formation (in order from the base to the top). For a more detailed lithology description, refer to *Regional Geology of the Hubei Province* [33].

The Yinshan Pb-Zn-Ag deposit (115°10'11"–115°11'19", 29°54'29"–29°53'58"), located in the southern region of the Edong district, lies within the MYRB (Figure 1b). The deposit is mainly comprised of Pb and Zn mineralization, in addition to Ag, Au, Cd, Fe and Mn, with 95 kt Pb @ 2.0%; 262 kt Zn @ 5.6%; 501.7 t Ag @ 107 g/t; 2 t Au @ 0.43 g/t; 1.2 kt Cd @ 261 ppm. It is situated on the south side of the east part of the Huanggushan-Xiniushan overturned anticline, and the ore body primarily occurs within the northwest interlayer

fracture zone located within the northern side of the Xiaojiawan-Xingjiawan syncline, as shown in Figure 2. The outcrop rocks in the orefield primarily consist of the lower Permian, middle Carboniferous, and middle Silurian strata, with the Devonian and Ordovician strata absent due to tectonic activity. The Silurian strata is primarily comprised of shale and sandstone (Fentou group,  $S_{1f}$ ). The upper part of Carboniferous strata (Huanglong Group,  $C_{2h}$ ) consists of limestone that gradually evolves into dolomite, which was subsequently deformed into breccia and is considered an ideal place for mineralization. The Permian strata is composed of the Qixia Group ( $P_{1q}$ ) of carbonaceous limestone and quartz sandstone, and the Maokou Group ( $P_{1m}$ ) of limestone. The granite porphyry is common but is primarily found in dykes (Figure 3). Chemical analyses show that the granite porphyry dykes have  $>0.2\%$  Pb + Zn content near the ore body, but only  $\sim 150$  ppm Pb and 200 ppm Zn far from the ore body (Edong Geological Survey, 1995).

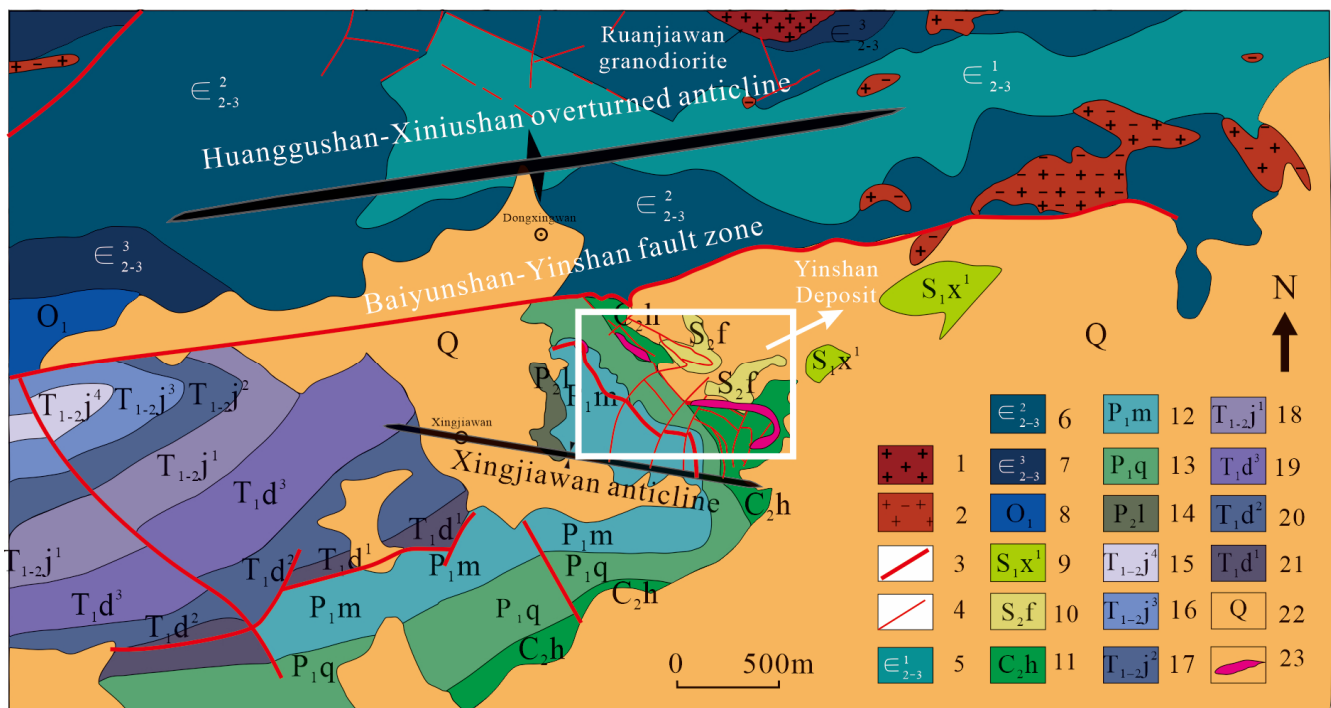


**Figure 2.** Schematic regional geological map of the Yinshan Pb-Zn-Ag deposit (modified from [10]). 1—Granodiorite; 2—Granodiorite porphyry; 3—main fault; 4—secondary fault; 5—1st member of the middle to upper Cambrian strata; 6—2nd member of the middle to upper Cambrian strata; 7—3rd member of the middle to upper Cambrian strata; 8—lower Ordovician strata; 9—Xintan Group of lower Silurian strata; 10—Fentou Group of middle Silurian strata; 11—Huanglong Group of middle Carboniferous strata; 12—Maokou Group of the lower Permian strata; 13—Qixia Group of the lower Permian strata; 14—Longtan Group of the middle Permian strata; 15—4th member of the Jialingjiang Group in the lower Triassic strata; 16—3rd member of the Jialingjiang Group in the lower Triassic strata; 17—2nd member of the Jialingjiang Group in the lower Triassic strata; 18—1st member of the Jialingjiang Group in the lower Triassic strata; 19—3rd member of the Daye Group in the lower Triassic strata; 20—2nd member of the Daye Group in the lower Triassic strata; 21—1st member of the Daye Group in the lower Triassic strata; 22—Quaternary strata; 23—Pb-Zn-Ag ore body.

The Yinshan deposit is comprised of five ore bodies, with the first ore body being the largest. The first ore body is located within the interlayer fracture zone between the Huanglong Group ( $C_{2h}$ ) and the Fentou Group ( $S_{1f}$ ), bound by  $F_1$  and  $F_2$  (Figure 4). As a result of post-mineralization tectonic activity, the ore body was uplifted and oxidated. This study specifically focuses on the sulfide minerals.

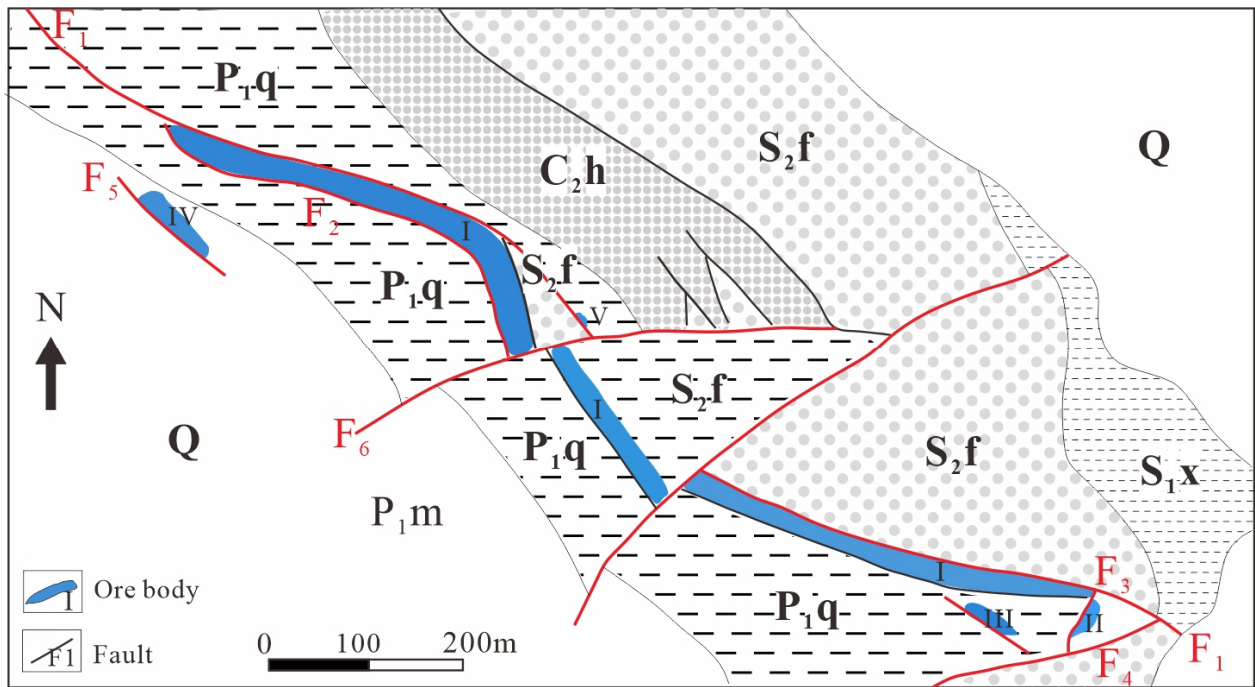


Figure 3. Geological map of the Yinshan Pb-Zn-Ag deposit (modified from Yan (2013) [10]). The abbreviation of the strata is the same as in Figure 2.

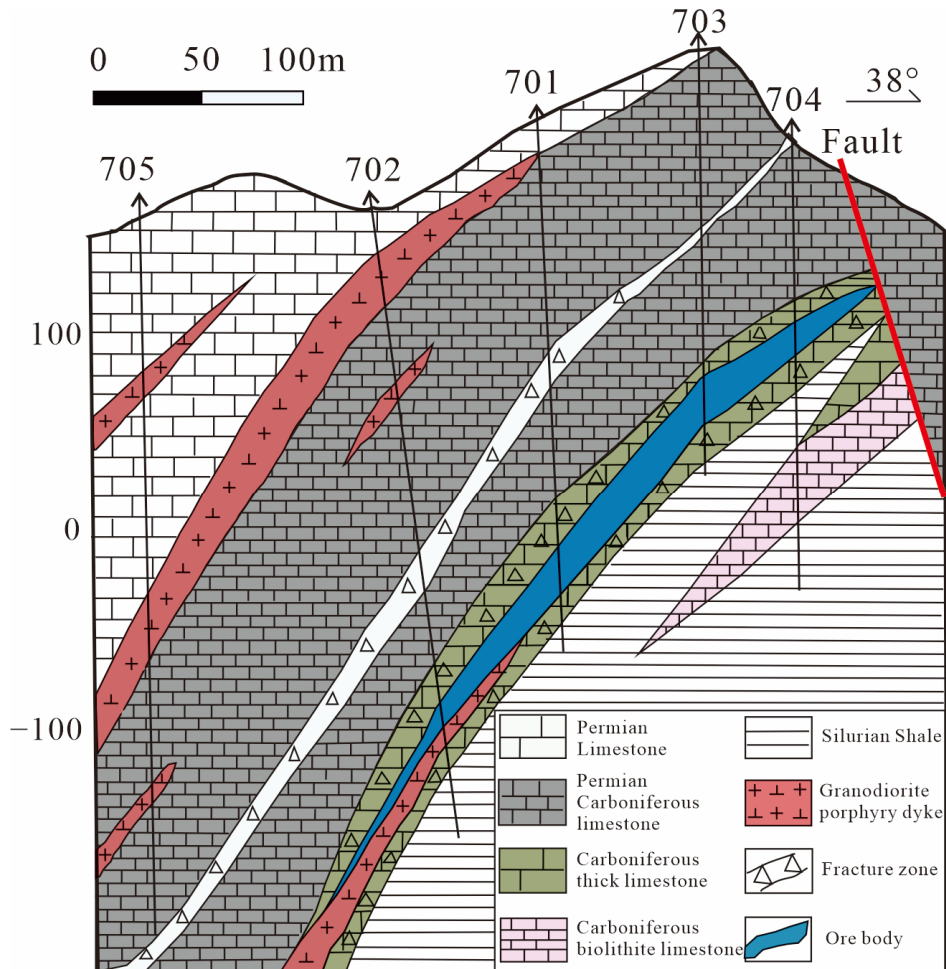
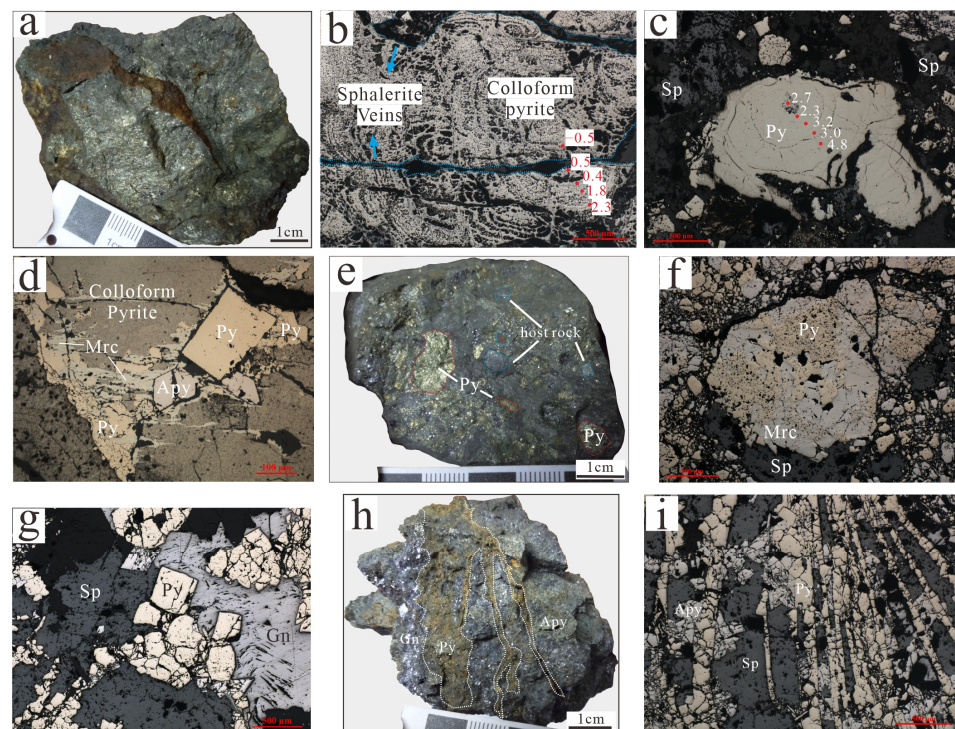


Figure 4. Geological map of Yinshan Pb-Zn-Ag deposit (modified from Yan (2013) [10]).

The sulfide mineralization at the Yinshan Pb-Zn-Ag deposit can be divided into two epochs: the pre-mineralization pyrite epoch and the hydrothermal mineralization epoch. The former primarily consists of colloform and massive pyrite, accompanied by minor marcasite (Figure 5a). Colloform pyrite exhibits varying amounts of non-sulfide minerals, displaying either a dirty or clean surface in polished thin sections (Figure 5b,c). These non-sulfide minerals may comprise detrital and authigenic minerals, including quartz, illite, dolomite and organic matter. Colloform pyrite has undergone replacement by massive pyrite, and both have been subsequently replaced by marcasite (Figure 5d,f). The sulfide minerals from the pre-mineralization epoch have undergone deformation, forming breccia and being cemented by sulfide minerals and gangue minerals from the hydrothermal epoch (Figure 5c,e,f). The hydrothermal mineralization epoch can be further divided into three stages: (1) The pyrite-arsenopyrite stage, characterized by the replacement of colloform and massive pyrite by euhedral pyrite and arsenopyrite along fractures; (2) The galena-sphalerite stage, in which galena and sphalerite formed in relatively open spaces compared to the pyrite-arsenopyrite stage, serving primarily as cement within the breccia. Polished sections reveal the progression of euhedral pyrite and arsenopyrite being replaced by galena, followed by subsequent replacement of galena by sphalerite (Figure 5g); (3) The vein pyrite stage, where straight pyrite veins cut across all preceding minerals (Figure 5h), exhibiting distinct and straight boundaries (Figure 5i).



**Figure 5.** (a) Colloform and massive pyrite ores; Reflected light photomicrographs shown that (b) Colloform pyrite containing non-sulfide minerals was cut by sphalerite veins; (c) Colloform pyrite with little non-sulfide minerals was replaced by sphalerite; (d) Colloform pyrite was replaced by massive pyrite, and they were both replaced by marcasite. Euhedral pyrite and arsenopyrite veins cut all the above minerals; (e) Hand specimen of breccia ores, with massive pyrite and host rock as breccia, and cemented by hydrothermal minerals, such as sphalerite, galena, and so on; Reflected light photomicrographs show that (f) the massive pyrite breccia were replaced by marcasite, and cemented by sphalerite; (g) The euhedral pyrite was replaced by galena and then sphalerite; (h) The hand specimen of the pyrite vein cut the early sulfide minerals, such as galena and arsenopyrite; (i) The pyrite vein cut through arsenopyrite and sphalerite in reflected light photomicrographs. The read scale bars represent 500  $\mu\text{m}$  in (b,c,f,g,i) and 100  $\mu\text{m}$  in (d). *Apy*—Arsenopyrite, *Gn*—Galena, *Mrc*—Marcasite, *Py*—Pyrite, *Sp*—Sphalerite.

Figure 6 provides a summary of the metallogenic epochs and stage, incorporating findings from previous studies. The mineralogy of the supergene epochs were referenced from Yan (2013) [10].

Stages Mineral	Pre-mineralization epoch		Hydrothermal mineralization epoch			Supergene epoch
	Stage 1	Stage 2	Stage 1	Stage 2	Stage 3	
			Pyrite + Arsenopyrite	Galena + Sphalerite	Vein Pyrite	
Colloform pyrite	█					
Massive pyrite	█					
Marcasite		█				
Pyrite			█		█	
Arsenopyrite			█			
Galena				█		
Sphalerite				█		
Psilomelane						█
Pyrolusite						█
Hematite						█
Goethite						█
limonite						█
Cerussite						█
Native silver						█
Mimetite						█
Malachite						█

Figure 6. Mineral paragenesis for the Yinshan Pb-Zn-Ag deposit.

### 3. Samples and Analytical Methods

To conduct the in-situ sulfur isotope study, we collected samples from different epochs and selected sulfide minerals from various stages for analysis. The selected samples with the least oxidation were divided into polished sections (~200 µm). Through detailed microscopic examination, sulfide minerals representing different stages were chosen for in-situ sulfur isotope analysis.

The sulfur isotope analysis was performed using in-situ methods at the State Key Laboratory of Geological Processes and Mineral Resources (GPMR, China University of Geosciences, Wuhan, China). The Nu Plasma II MC-ICP-MS was employed, equipped with a Resonetics-S155 excimer ArF laser ablation system. The laser beam had a diameter of 33 µm and operated at a repetition rate of 10 Hz, with each ablation process lasting 40 s. To determine the  $\delta^{34}\text{S}$  values, we employed the standard-sample bracketing (SSB) technique throughout the MC-ICP-MS analytical sessions [38]. Instrumental mass bias correction was carried out by linearly interpolating the biases calculated from two adjacent standard analyses, enabling accurate calculation of the true sulfur isotope values. The isotope data are reported in delta notation (‰) relative to Vienna Cañon Diablo Troilite (V-CDT):

$$\delta^{34}\text{S}_{\text{V-CDT}} = [((^{34}\text{S}/^{32}\text{S})_{\text{sample}} / (^{34}\text{S}/^{32}\text{S})_{\text{V-CDT}}) - 1] \times 10^3$$

where  $(^{34}\text{S}/^{32}\text{S})_{\text{sample}}$  is the measured  $^{34}\text{S}/^{32}\text{S}$  ratio in the sample and  $(^{34}\text{S}/^{32}\text{S})_{\text{V-CDT}}$  is defined as 0.044163 [39]. The analytical precision ( $2\sigma$ ) was estimated to be  $\pm 0.2$  per mil.

The laboratory's internal standards were calibrated using international standards, including a sphalerite standard (NBS-123) and two pyrite standards (WS-1 and WS-2). NBS-123 served as the reference standard for sphalerite and yielded a  $\delta^{34}\text{S}$  value of  $+17.1 \pm 0.1$ ‰. WS-1 and WS-2 were natural pyrite samples collected from the Wenshan polymetallic skarn deposit in Yunnan Province, China. WS-1 was utilized as the reference standard for pyrite, galena, marcasite and arsenopyrite, while WS-2 served as the monitor standard. The  $\delta^{34}\text{S}$  values for WS-1 and WS-2 were determined at GPMR, China University of Geosciences, and were found to be  $+0.9$ ‰ and  $+2.0$ ‰, respectively.

### 4. Results

The detailed sulfur isotope data are shown in Table 1 and Figure 7.

**Table 1.** The in-situ sulfur isotope data of sulfide minerals in Yinshan Pb-Zn-Ag deposit.

Epoch	Stage	Sulfide Mineral	$\delta^{34}\text{S}$ Value (‰)	Comment	
The pre-mineralization pyrite	Colloform pyrite	Pyrite	−0.5	Grain 1, spot 1	
		Pyrite	0.5	Grain 1, spot 2	
		Pyrite	−0.4	Grain 1, spot 3	
		Pyrite	1.8	Grain 1, spot 4	
		Pyrite	2.3	Grain 1, spot 5	
		Pyrite	2.7	Grain 2, spot 1	
		Pyrite	2.3	Grain 2, spot 2	
		Pyrite	3.2	Grain 2, spot 3	
		Pyrite	3.0	Grain 2, spot 4	
		Pyrite	4.8	Grain 2, spot 5	
	Massive pyrite	Pyrite	1.0		
		Pyrite	1.8		
		Pyrite	2.2		
		Pyrite	2.2		
		Pyrite	2.5		
		Pyrite	2.5		
		Pyrite	2.6		
		Pyrite	2.7		
		Pyrite	2.9		
		Pyrite	3.0		
		Pyrite	3.0		
		Pyrite	3.0		
		Pyrite	3.0		
		Pyrite	3.1		
		Pyrite	3.1		
		Pyrite	3.3		
		Pyrite	3.4		
		Pyrite	3.6		
	Pyrite	3.7			
	Marcasite		Marcasite	1.9	
			Marcasite	2.5	
			Marcasite	3.1	
Marcasite			3.6		
The hydrothermal mineralization	The euhedral pyrite and arsenopyrite	Arsenopyrite	2.2		
		Arsenopyrite	2.4		
		Arsenopyrite	2.6		
		Arsenopyrite	4.8		
		Arsenopyrite	6.3		
		Arsenopyrite	3.1		
		Arsenopyrite	3.5		
		Arsenopyrite	2.7		
		Arsenopyrite	3.4		
		Arsenopyrite	4.3		
		Arsenopyrite	3.7		
		Arsenopyrite	4.2		
		Arsenopyrite	3.5		
		Arsenopyrite	4.5		
		Arsenopyrite	4.5		
		Arsenopyrite	4.9		
		Arsenopyrite	4.2		
		Arsenopyrite	4.2		
Pyrite	3.7				
Pyrite	3.3				
Pyrite	2.7				
Pyrite	3.1				
Pyrite	2.6				

Table 1. Cont.

Epoch	Stage	Sulfide Mineral	$\delta^{34}\text{S}$ Value (‰)	Comment
		Sphalerite	4.5	
		Sphalerite	4.4	
		Sphalerite	5.2	
		Sphalerite	4.7	
		Sphalerite	4.2	
		Sphalerite	4.8	
		Sphalerite	6.5	
		Sphalerite	6.5	
		Sphalerite	6.2	
		Sphalerite	4.4	
		Sphalerite	4.6	
		Sphalerite	4.3	
		Sphalerite	2.9	
	The Galena-Sphalerite	Sphalerite	4.5	
		Sphalerite	4.4	
		Galena	3.0	
		Galena	4.6	
		Galena	7.1	
		Galena	5.7	
		Galena	5.9	
		Galena	5.0	
		Galena	5.4	
		Galena	2.6	
		Galena	2.0	
		Galena	2.5	
		Galena	2.6	
		Galena	2.0	
		Galena	1.1	
		Pyrite	2.1	
		Pyrite	2.1	
	The vein pyrite	Pyrite	2.4	
		Pyrite	3.2	
		Pyrite	3.4	
		Pyrite	3.5	
		Pyrite	3.8	

Regarding the pre-mineralization sulfide minerals, it is noteworthy that the colloform pyrite exhibits a gradual increase in  $\delta^{34}\text{S}$  values towards the edge of the grain, with values ranging from  $-0.5$  to  $2.3$ ‰ and  $2.7$  to  $4.8$ ‰, respectively. Similarly, the massive pyrite shows a narrow range of  $\delta^{34}\text{S}$  values, ranging from  $1.0$  to  $3.7$ ‰, with the majority falling between  $2.5$  and  $3.7$ ‰. The marcasite also displays similar  $\delta^{34}\text{S}$  values, ranging from  $1.9$  to  $3.6$ ‰ (Figure 7a). In contrast, the hydrothermal sulfide minerals exhibit larger variations in  $\delta^{34}\text{S}$  values compared to the pre-mineralization sulfide minerals (Figure 7). The  $\delta^{34}\text{S}$  values of the euhedral pyrite-arsenopyrite stage range from  $2.2$  to  $4.9$ ‰, with one exception of  $6.3$ ‰ (Figure 7b). The  $\delta^{34}\text{S}$  values of the galena-sphalerite stage exhibit a bimodal distribution, with a range of  $1.1$ – $3.0$ ‰ and  $4.2$ – $7.1$ ‰, respectively (Figure 7c). Finally, the vein pyrite stage displays the lowest  $\delta^{34}\text{S}$  values, ranging from  $2.1$  to  $3.8$ ‰ (Figure 7d).

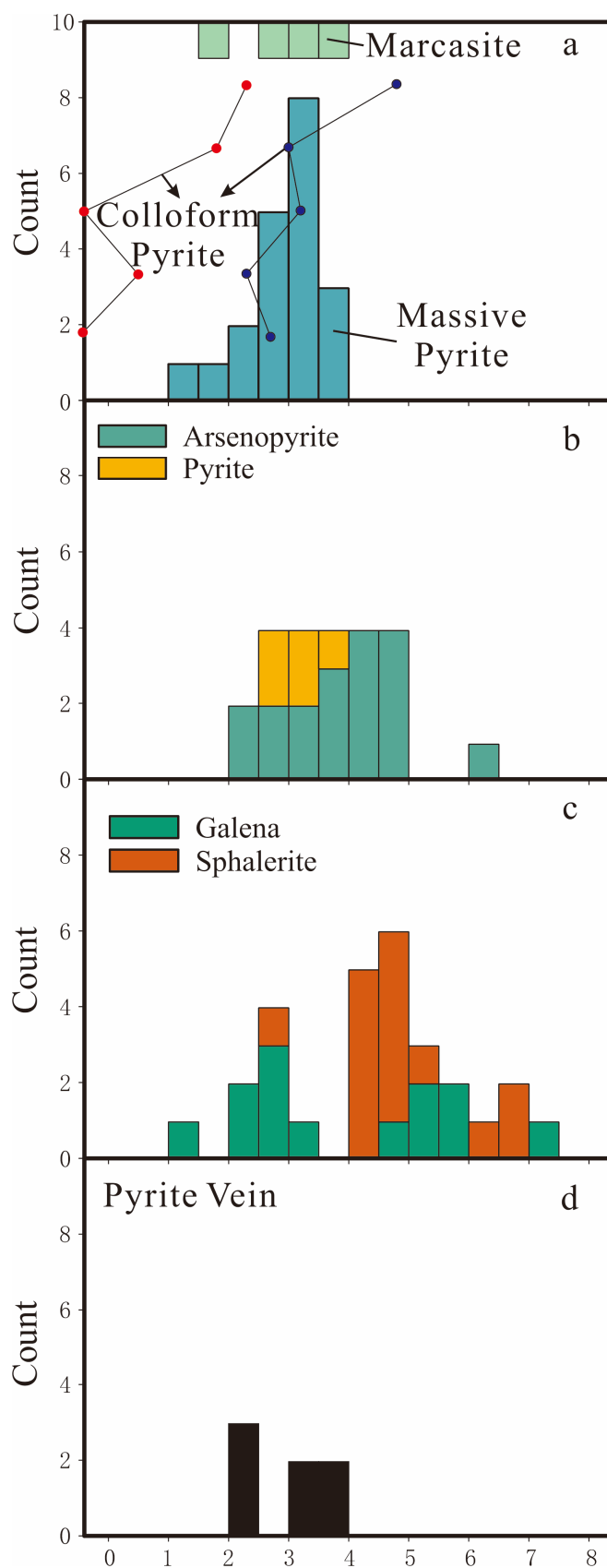


**Figure 7.** Histograms of sulfur isotopes for sulfide minerals from different epochs and stages. (a) The pre-mineralization pyrite epoch, followed by (b) the pyrite-arsenopyrite stage, (c) the galena-sphalerite stage, and (d) the vein pyrite stage during the hydrothermal mineralization epoch.

## 5. Discussion

### 5.1. Source of Sulfur

The  $\delta^{34}\text{S}$  values of both colloform and massive pyrite in this study range from  $-0.5$  to  $4.8\%$  (Figure 7a), which is similar to the observations in the Qixiashan Pb-Zn-Ag polymetallic deposit [24]. The presence of detrital and authigenic minerals, such as quartz, illite, dolomite and organic matter in colloform pyrite ores suggests their formation under euxinic marine sedimentary conditions during the Hercynian period [40].

During the hydrothermal epoch, the narrow range of sulfur isotope values at all stages suggests an equilibrium between sulfide minerals and the hydrothermal fluid. The absence of sulfate minerals indicates that the sulfur in the hydrothermal fluid was mainly in the form  $\text{H}_n\text{S}^{n-2}$  [41–43]. The sulfur isotope composition of sulfide minerals can represent the composition of the hydrothermal fluid [44,45]. Within the same stage, paired sulfide minerals were analyzed, but the equilibrium composition was not determined. Euhedral pyrite and arsenopyrite represent the initial sulfide mineral precipitation during mineralization, followed by the formation of breccia during the transition to the galena-sphalerite stage, which coincided with fluid boiling. The alternating characteristics of Hercynian sulfide minerals are limited in extent and distribution, and there is no significant deposition of sulfide minerals after the pyrite-arsenopyrite stage. This suggests the Hercynian sulfide minerals contribute minor amounts of sulfur, insufficient to precipitate significant sulfur minerals. Although organic matter may also provide some reduced sulfur during alteration [44], the significantly lower abundance compared to sulfide minerals diminishes its importance in the process of mineral precipitation. Despite significant overlap, the sulfur isotope values of pyrite and arsenopyrite (stage 1) are relatively higher than those of Hercynian sulfide minerals (Figure 7a,b). The decrease in sulfur isotope values (Figure 7b) could be attributed to both the assimilation of Hercynian sulfur and Rayleigh fractionation of pyrite and arsenopyrite, but properly evaluating the relative importance of these factors is challenging.

During the galena and sphalerite stage, the boiling of hydrothermal fluids resulted in the degassing of  $\text{H}_2$  and  $\text{H}_2\text{S}$ , thereby increasing the  $f\text{O}_2$  and decreasing the  $f\text{S}_2$  in the residual liquid [46]. This process efficiently fractionated elements due to the segregation of vapor and liquid phases. The  $\delta^{34}\text{H}_2\text{S}$  composition of the fluid (and coexisting vapor) likely decreased due to the preferential oxidation of  $\text{H}_2^{34}\text{S}$  during boiling [46,47]. As a result, some sphalerite and galena exhibit lower sulfur isotope values [48,49] compared to the euhedral pyrite-arsenopyrite stage (Figure 7b,c). During the crystallization of sphalerite and galena, the  $\delta^{34}\text{S}$  values increased, likely due to Rayleigh fractionation of galena, which preferentially incorporates lighter  $^{32}\text{S}$  [43], or due to the assimilation of sulfur from massive pyrite. Galena formed relatively earlier than sphalerite, consistent with Rayleigh fractionation. Both pyrite and sphalerite prefer heavier  $^{34}\text{S}$  than  $\text{H}_2\text{S}$ , but pyrite has a higher preference [43]. The decrease in  $\delta^{34}\text{S}$  values from the galena-sphalerite stage to the vein pyrite stage may be attributed to the Rayleigh fractionation of sphalerite, which removes the heavier  $^{34}\text{S}$ .

The  $\delta^{34}\text{S}$  values exhibit variation among different geological reservoirs: (1) meteorites typically show values near  $0\%$ , (2) igneous rocks range from  $-2\%$  to  $8\%$ , (3) modern and ancient biogenic pyrite display values between  $-20\%$  and  $+20\%$  [43], and (4) anhydrite in MYRB demonstrates values from  $+21.1\%$  to  $+34.4\%$  [50–52]. The  $\delta^{34}\text{S}$  value of the ore-forming fluid is estimated to be around  $0\text{--}5\%$ , indicating a likely origin from magma, as magmatic sulfur shares similar  $\delta^{34}\text{S}$  values. This finding aligns with the conclusions drawn from trace element data of sulfide minerals [10]. However, it is plausible that sulfide minerals formed during the Hercynian period also made some contribution.

### 5.2. Contribution of Colloform and Massive Pyrite to Mineralization

In the Yangtze River Metallogenic belt, it is expected that Pb-Zn-Ag deposits in the other districts share similar metallogenic processes with the Yinshan deposit [2,3,5,6,11–19,21–25]. Comparisons to other deposits can provide insights into the controlling factors influencing Pb-Zn mineralization. Overprinting of Hercynian

stratabound sulfides is only reported in the Baiyangfan Pb-Zn-Ag deposit in the Jiurui district [21,22] and the Qixiashan Pb-Zn-Ag deposit in Ningzhen district [23–25]. However, in most other deposits, Pb-Zn ore bodies typically develop in weak zones of the host rock, such as the interlayer fracture zone between clastic and carbonate rocks, as observed in the Huangshanling Pb-Zn-Ag-Mo deposit in Anqing-Guichi district [11–13], the Qixiashan Pb-Zn deposit in the Ningzhen district [23–25], or in volcanic sedimentary rock, as seen in the Yueshan Ag-Pb-Zn deposit [14,16,17]. Another example of this development can be found in fault zones, as seen in the Hehuashan Pb-Zn deposit [6]. The absence of a preference for a specific stratum indicates that the alternation of Hercynian stratabound sulfide, i.e., colloform and massive pyrite, may contribute in part to the ore-forming element and promote the precipitation of sulfide minerals, but these sulfide materials are not the decisive factor. In fact, the ore bodies of the Yinshan Pb-Zn-Ag deposit are also located at the interface of Carbonaceous clastic rock and Carbonaceous-Permian carbonate rock, where the interlayer fracture zone is an ideal site for Pb-Zn mineralization due to the discrepancy in lithology. Sphalerite and galena crystallize following fluid boiling, rather than during the initial alternation of colloform and massive pyrite. This suggests that the alternation of colloform and massive pyrite does not play a prominent role in controlling mineralization.

### 5.3. Possible Parental Magma of Pb-Zn Mineralization in Yinshan Deposit

The previous understanding of the Yinshan Pb-Zn deposit suggested it was a distal skarn Pb-Zn associated with the Ruanjiawan Cu-W skarn deposit [10]. However, recent in-situ sulfur studies conducted for the Ruanjiawan Cu-W skarn deposit have revealed an increase in sulfur isotopes from ~0‰ to ~15‰ towards the host rock, suggesting the assimilation of evaporite [53]. If the Ruanjiawan intrusion were the parent rock of the Yinshan deposit, its sulfur isotope signature would be significantly higher than what was observed in this study. Additionally, the granodiorite porphyry in the orefield has undergone alteration by Pb-Zn hydrothermal fluids, as evidenced by the higher Pb and Zn content (>0.2% Pb + Zn) in dykes closer to the ore body, eliminating the possibility of it being the parental magma source. Therefore, it is reasonable to assume the presence of a hidden magma body beneath the Yinshan deposit.

Although no absolute radiogenic age was determined in this study, the relative rock- and ore-forming age can be inferred based on geological evidence. The inference relies on the understanding that the rocks and minerals with different origins or closure temperatures can record geological processes of different ages. The Ruanjiawan granodiorite and Xiniushan granodiorite porphyry, located north of the Yinshan deposit (Figure 3), have zircon U-Pb ages of  $143 \pm 1$  Ma and  $147 \pm 1$  Ma, respectively [54]. Since the granodiorite porphyry dykes in the Yinshan orefield resemble the Ruanjiawan and Xiniushan magmatic rocks, it is likely that the mineralization age of the Yinshan deposit is later than 147 Ma. Notably, the titanite in the Ruanjiawan granodiorite measures a U-Pb age of  $132 \pm 1$  Ma, which is more than 10 Ma later than the zircon U-Pb age and titanite U-Pb age in the skarn ( $142 \pm 2$  Ma). This age difference suggests a thermal overprinting event associated with diabase dyke emplacement (Zircon U-Pb age of  $133 \pm 1$  Ma) [55]. Therefore, magmatic activity around ~133 Ma is present in the Ruanjiawan-Yinshan area. However, since there is no exposed felsic magma body in the Yinshan deposit at ~133 Ma, the parental magma characteristics can only be evaluated by comparing them with the Pb-Zn deposit in the MYRB, assuming that all of these Pb-Zn deposits share a similar origin.

Isotopic and trace element studies conducted on sulfide minerals in other Pb-Zn deposits within the MYRB consistently indicate a significant contribution from magmatic fluid [2,3,5–8,11–17,19,21–25]. The Huangshanling and Yaojialing deposits, with well-exposed ore bodies and magmatic rocks, serve as ideal examples for examining the parental magma of Pb-Zn mineralization. The Huangshanling Pb-Zn-Ag-Mo deposit in the Anqing-Guichi district shares geological characteristics with the Yinshan deposit. Quartz diorite porphyry dykes were found at shallow depths replacing skarn minerals [12], while deeper granite porphyries with A-type granite characters were also discovered. The diorite por-

phyry dykes exhibit zircon U-Pb ages of  $144 \pm 1.4$  Ma [12] or  $137 \pm 1.5$  Ma [13], whereas the granite porphyry has a zircon U-Pb age over 10 million years younger, at  $125 \pm 1.2$  Ma. The molybdenite Re-Os age of 127.5 Ma suggests a relationship between mineralization and the deep granite porphyry [11]. Pb-Zn-Ag mineralization develops in the shallow interlay fracture zone between clastic and carbonate rocks [12,13], while Mo mineralization takes place at greater depths near the granite porphyry.

In the Yaojialing deposit, the Pb-Zn ore body is closely situated to granodiorite porphyry, similar to the formation of Cu-Au mineralization [2,3,5,7,8]. Previous studies have proposed a connection between Pb-Zn mineralization and granodiorite porphyry based on the similarity of granite zircon U-Pb ages ( $\sim 141$  Ma [2,7,8]) and molybdenite Re-Os ages ( $\sim 142$  Ma [2,5]) in the Yaojialing Pb-Zn deposit. However, this conclusion assumes that Pb-Zn and Cu-Au mineralization occurred simultaneously. The proximity of the Pb-Zn ore body to the parental magmatic rock only occurs when the granite exhibits a high concentration of F, which lowers the solidus temperature of magma, resulting in the formation of low-temperature hydrothermal fluid. These fluids need to have a sufficiently low temperature for Pb-Zn to exhibit low solubility and precipitate, as observed in the Empire Cu-Zn Mine in Idaho [56,57]. However, the granodiorite porphyry in Yaojialing does not display elevated F levels, and it is evident that numerous Pb-Zn veins cut through the granodiorite rock [3]. Therefore, it is likely that the Pb-Zn mineralization in Yaojialing is associated with a later magmatic-hydrothermal event. Furthermore, in addition to the  $\sim 141$  Ma granodiorite, late-stage granodiorite porphyry dykes with an age of  $130.3 \pm 1.5$  Ma have also been reported [4], resembling the situation in the Huangshanling Pb-Zn-Ag-Mo deposit. The Pb-Zn mineralization in Yaojialing may be related to the  $\sim 130$  Ma magmatism.

Based on the aforementioned findings, it can be inferred that the Pb-Zn (Ag) deposit in the Yangtze River Metallogenic belt is associated with a magmatic event that took place approximately 133 Ma ago.

#### 5.4. Ore Genesis and Its Implications for Exploration Strategies

Based on the preceding discussion, we propose a revised model for the ore genesis of the Yinshan Pb-Zn-Ag deposit. Our model suggests that the mineralization can be divided into two distinct stages: the sedimentary stage and the hydrothermal stage, each characterized by different processes. During the Hercynian period, colloform and massive pyrite formed in the sedimentary stage [40]. In the early Cretaceous period, a granite intrusion was emplaced at a deep level, around 130 Ma. This intrusion released ore-forming fluid, leading to the formation of Mo mineralization in close proximity to the magma rock. These hydrothermal fluids, originating from the deep magma, were likely enriched in oxidized sulfur species, primarily composed of  $\text{SO}_2$ . However, during retrograde alteration, magnetite formation occurred, reducing the fluid's oxygen fugacity ( $f_{\text{O}_2}$ ) and transforming  $\text{SO}_2$  into  $\text{H}_2\text{S}$ . This process provided the necessary reduced level of sulfur for Mo mineralization. As Mo has a higher depositional temperature compared to Pb-Zn, the fluid still retained significant concentrations of Pb-Zn after Mo mineralization. As the remaining hydrothermal fluid ascended and reached the interface between carbonate and shale rocks, boiling of the fluid occurred, resulting in its cooling. This decrease in temperature led to a significant drop in the solubility of Pb-Zn, causing the precipitation of galena and sphalerite. It is important to note that the alternation of colloform and massive pyrite may contribute to the content of reduced sulfur in the fluid and promote the crystallization of sphalerite and galena.

The genetic relationship between distal epithermal Pb-Zn mineralization and proximal Mo or other mineralization is widely recognized in other deposits [58–62]. Pb-Zn mineralization can serve as a useful indicator for the presence of proximal mineralization. In the case of the Yinshan deposit, the occurrence of shallow Pb-Zn-Ag mineralization suggests the potential presence of deeper Mo mineralization. However, the exploration target for deep Mo mineralization has been narrowed down by the surface occurrence of

Pb-Zn mineralization. Geophysical prospecting techniques, therefore, play a crucial role in identifying hidden magmatic rocks and expanding exploration targets.

## 6. Conclusions

After a thorough analysis of the Yinshan Pb-Zn-Ag deposit, we have concluded that the sulfide isotope composition of the deposit indicates a magmatic origin. Furthermore, the geological features suggest that the mineralization is associated with a ~130 Ma granite. Although the colloform and massive pyrite formed during the Hercynian period, they may still have contributed to the mineralization and are not the primary controlling factors. Our findings suggest that there is likely Mo mineralization at a deeper level, which is consistent with the presence of Pb-Zn mineralization in the Yangtze River Metallogenic belt. Overall, our research provides valuable insights into the mineralization process of the Yinshan Pb-Zn-Ag deposit and sheds light on the potential for further exploration of Mo mineralization in the area.

**Author Contributions:** Writing—original draft preparation, D.D., H.J. and Y.W.; writing—review and editing, D.D., H.J. and Y.W. All authors have read and agreed to the published version of the manuscript.

**Funding:** This research was funded by the National Natural Science Foundation of China, grant number 42172088 and 42203065 and Natural Science Foundation of Hubei Province, grant number 2019CFB586.

**Data Availability Statement:** The data presented in this study are available within the article.

**Acknowledgments:** We thank the editor and reviewers for their constructive comments which helped in improving our paper.

**Conflicts of Interest:** The authors declare no conflict of interest.

## References

1. Mao, J.; Xie, G.; Duan, C.; Pirajno, F.; Ishiyama, D.; Chen, Y. A Tectono-Genetic Model for Porphyry–Skarn–Stratabound Cu–Au–Mo–Fe and Magnetite–Apatite Deposits along the Middle–Lower Yangtze River Valley, Eastern China. *Ore Geol. Rev.* **2011**, *43*, 294–314. [[CrossRef](#)]
2. Zhong, G.X.; Zhou, T.F.; Yuan, F.; Jiang, Q.S.; Fan, Y.; Zhang, D.Y.; Huang, J.M. LA-ICPMS U–Pb Zircon Age and Molybdenite Re–Os Dating of Yaojialing Large Zinc–Gold Polymetallic Deposits, Tongling, Anhui Province, China. *Acta Petrol. Sin.* **2014**, *30*, 1075–1086. (In Chinese)
3. Liu, S.F. The Metallogenesis Research of Yaojialing Zn–Au Polymetallic Deposit in Tongling, Anhui Province. Ph.D. Thesis, China University of Geosciences (Beijing), Beijing, China, 2012. (In Chinese).
4. Liu, Z. The Petrogenesis and Metallogenesis of the Yaojialing Polymetallic Zn–Au Deposit in Tongling City, Anhui Province. Master’s Thesis, Hefei University of Technology, Hefei, China, 2016. (In Chinese).
5. Yin, Y.D.; Hong, T.Q.; Jia, Z.H.; Zhao, H.; Li, C.; Luo, L.; Huang, J.M. The Re–Os Age of Molybdenite and Ore-Forming Material Source from the Yaojialing Zn–Au Polymetallic Deposit, Tongling. *Geol. Rev.* **2016**, *62*, 248–256. (In Chinese)
6. Liu, G.X.; Yuan, F.; Deng, Y.F. The sphalerite trace element and ore forming fluid character of Hehuashan Pb–Zn deposit, Tongling district, Anhui province. In Proceedings of the ninth National Symposium on Metallogenic Theory and Prospecting Methods, Nanjing, China, 13–16 December 2019; pp. 27–28. (In Chinese).
7. Liu, S.F.; Du, Y.S.; Fu, S.X.; Zhong, H.; Cao, Y. U–Pb Age and Hf Isotopic Characteristics of Zircons from Granodiorite Porphyry in the Yaojialing Zn–Au Polymetallic Mine, Anhui Province and Their Geological Significance. *Earth Sci.-J. China Univ. Geosci.* **2013**, *38*, 91–102. (In Chinese)
8. Liu, J.M.; Yan, J.; Li, Q.Z.; Song, C.Z.; Liu, X.Q.; Xie, J.C. Zircon Dating and Petrogenesis of the Yaojialing Intrusion in Tongling Area. *Chin. J. Geol.* **2014**, *49*, 494–512. (In Chinese)
9. Meinert, L.D.; Dipple, G.M.; Nicolescu, S. World Skarn Deposits. In *One Hundredth Anniversary Volume*; Hedenquist, J.W., Thompson, J.F.H., Goldfarb, R.J., Richards, J.P., Eds.; Society of Economic Geologists: Littleton, CO, USA, 2005; pp. 299–336. ISBN 978-1-887483-01-8.
10. Yan, D.R. Geological Characteristics and Genesis of the Ruanjiawan Cu–Mo–W and Yinshan Pb–Zn–Ag Deposits. Ph.D. Thesis, China University of Geosciences, Wuhan, China, 2013. (In Chinese).
11. Chen, X.F. Ore-Forming System of Guilinzheng–Huangshanling Deposit in Jiangnan Transitional Zone. Master’s Thesis, Hefei University of Technology, Hefei, China, 2016. (In Chinese).

12. Tian, K. The origin of Huangshanling Pb-Zn-Mo deposit, Guichi district, Anhui province: Evidence from zircon U-Pb and Pb isotope study. In Proceedings of the Topic 1: Meso-Cenozoic Large Scale Mineralization and Prospecting in Eastern China, Changsha, China, 11–14 December 2015; Volume S1, p. 59. (In Chinese).
13. Zuo, N. Study on Geological Characteristics and Genesis of the Huangshanling Pb-Zn-Mo Deposit in Chizhou, Anhui Province. Master's Thesis, China University of Mining & Technology, Xuzhou, China, 2018. (In Chinese).
14. Ge, N.J.; Li, P.; Huang, X.A.; Zhang, S.B.; Han, Z.Y. Research on physical chemistry condition and materials source of mineralization of Ag-Pb-Zn ore deposit in Yueshan. *J. China Univ. Sci. Technol.* **1989**, *19*, 365–374. (In Chinese)
15. Lan, B.Y.; Yuan, F.; Deng, Y.F.; Cheng, P.S.; Li, X.H.; Zhang, J.M.; Li, Z. In situ trace element composition of sphalerite and ore-forming fluid characteristics of Xiwan Pb-Zn deposit, Anhui Province. *Miner. Depos.* **2023**, *42*, 192–210. (In Chinese)
16. Qian, B.; Yuan, F.; Zhou, T.F.; Fan, Y.; Zhang, L.J.; Ma, L. The geological character and sulfur isotope geochemical study on Yueshan Ag-Pb-Zn deposit, Luzong basin. In *Proceedings of the Topic 9: Geochemical Tracers of Mineralization and Metallogenic Chronology*; Mineral Deposits: Changchun, China, 2010; Volume S1. (In Chinese)
17. Zha, S.X.; Han, Z.Y. Geochemical characteristics and genetic study of Yueshan Ag-Pb-Zn deposit, Anhui. *Resour. Surv. Environ.* **2002**, *23*, 272–280. (In Chinese)
18. Zhang, H.Q.; Han, S.C.; Zhang, Y.; Pan, J.Y.; Zhang, Y.Q.; Zhao, B.B.; Ding, Y.; Jiang, Y.; Hu, S.P. Trace element characteristics and geological significance of sphalerite in Xiwan lead-zinc deposit, Luzong Basin, Anhui Province. *Geol. J. China Univ.* **2022**. (In Chinese) [[CrossRef](#)]
19. Zhang, Y.Q. Research on the geochemical characteristic and genesis of the Xiwan lead-zinc deposit in Anhui Province. Master's Thesis, East China University of Technology, Nanchang, China, 2019. (In Chinese).
20. Liu, G.; Deng, Y.; Yuan, F.; Chen, X.; Yang, B. Rb–Sr Dating and S–Sr–Nd Isotopic Constraints on the Genesis of the Hehuashan Pb–Zn Deposit in the Middle–Lower Yangtze River Metallogenic Belt, China. *Solid Earth Sci.* **2021**, *6*, 57–69. [[CrossRef](#)]
21. Jia, L.; Yang, D.; Wang, L.; Long, N. Discussion on characteristics and mineralization of Yanshanian medium-low temperature thermal fluid system in Jiujiang-Ruichang ore concentration area, Jiangxi province. *China Min. Mag.* **2018**, *27* (Suppl. S1), 191–196+210. (In Chinese)
22. Zhong, H.; Xu, Y.M.; Gao, R.; Dong, Y.Y.; Zhang, L. *On Characteristics of Sulfides and Sulfur Lead Isotopic and Trace Elements of the Baiyangfan Lead-Zinc-Silver Deposit in the Jiurui Ore Concentration Area of Jiangxi Province*, 2016th ed.; Jiangxi Science and Technology Press: Nanchang, China, 2016. (In Chinese)
23. Sun, X.J.; Ni, P.; Yang, Y.L.; Qin, H.; Chen, H.; Gui, C.J.; Jing, S. Formation of the Qixiashan Pb–Zn Deposit in Middle-Lower Yangtze River Valley, Eastern China: Insights from Fluid Inclusions and in Situ LA-ICP-MS Sulfur Isotope Data. *J. Geochem. Explor.* **2018**, *192*, 45–59. [[CrossRef](#)]
24. Zhang, W.D.; Li, B.; Lu, A.H.; Zhao, K.D.; Elatikpo, S.M.; Chen, X.D.; Zhu, L.; Yu, M. In-Situ Pyrite Trace Element and Sulfur Isotope Characteristics and Metallogenic Implications of the Qixiashan Pb-Zn-Ag Polymetallic Deposit, Eastern China. *Ore Geol. Rev.* **2022**, *144*, 104849. [[CrossRef](#)]
25. Zhang, W.D.; You, H.T.; Li, B.; Zhao, K.D.; Chen, X.D.; Zhu, L. Ore-Forming Processes of the Qixiashan Carbonate-Hosted Pb-Zn Deposit, South China: Constraints from Sulfide Trace Elements and Sulfur Isotopes. *Ore Geol. Rev.* **2022**, *143*, 104786. [[CrossRef](#)]
26. Xie, S.C.; Yin, H.F. Biometallogenesis of Pb-Zn-Ag Polymetallic Deposit of Qixiashan in Nanjing. *Geol. J. China Univ.* **1997**, *16*, 65–74. (In Chinese)
27. Xie, S.C.; Yin, H.F.; Wang, H.M.; Zhou, X.G.; Zhang, W.H. Characteristics of Ore-Forming Fluids in Pb-Zn-Ag Polymetallic Deposit, Qixiashan, Nanjing. *Geol. Sci. Technol. Inf.* **1998**, *42* (Suppl. S1), 78–81. (In Chinese)
28. Junquan, L.; Qiuming, T.; Jiangzhou, L. *Metallogenic Series of Deposits in Hubei Province*; Hubei Science & Technology Press: Wuhan, China, 2005. (In Chinese)
29. Bendall, C.; Lahaye, Y.; Fiebig, J.; Weyer, S.; Brey, G.P. In Situ Sulfur Isotope Analysis by Laser Ablation MC-ICPMS. *Appl. Geochem.* **2006**, *21*, 782–787. [[CrossRef](#)]
30. Chang, Y.F.; Liu, X.P.; Wu, Y.C. *The cOpper-Iron Belt of the Lower and Middle Reaches of the Changjiang River*; Geology Publication House: Beijing, China, 1991. (In Chinese)
31. Xie, G.; Mao, J.; Xiongwei, L.; Duan, C.; Yao, L. Late Mesozoic Bimodal Volcanic Rocks in the Jinniu Basin, Middle–Lower Yangtze River Belt (YRB), East China: Age, Petrogenesis and Tectonic Implications. *Lithos* **2011**, *127*, 144–164. [[CrossRef](#)]
32. Shu, Q.A.; Chen, P.L.; Cheng, J.R. *Geology of Iron-Copper Deposits in Eastern Hubei Province*; Press of Metallurgical Industry: Beijing, China, 1992. (In Chinese)
33. Hubei Bureau of Geology. *Mineral Resources Regional Geology of Hubei Province*; Geological Publishing House: Beijing, China, 1990. (In Chinese)
34. Li, J.W.; Zhao, X.F.; Zhou, M.F.; Ma, C.Q.; de Souza, Z.S.; Vasconcelos, P. Late Mesozoic Magmatism from the Daye Region, Eastern China: U–Pb Ages, Petrogenesis, and Geodynamic Implications. *Contrib. Mineral. Petrol.* **2009**, *157*, 383–409. [[CrossRef](#)]
35. Li, J.W.; Vasconcelos, P.M.; Zhou, M.F.; Deng, X.D.; Cohen, B.; Bi, S.J.; Zhao, X.F.; Selby, D. Longevity of Magmatic–Hydrothermal Systems in the Daye Cu–Fe–Au District, Eastern China with Implications for Mineral Exploration. *Ore Geol. Rev.* **2014**, *57*, 375–392. [[CrossRef](#)]
36. Xie, G.; Mao, J.; Zhao, H. Zircon U–Pb Geochronological and Hf Isotopic Constraints on Petrogenesis of Late Mesozoic Intrusions in the Southeast Hubei Province, Middle–Lower Yangtze River Belt (MLYRB), East China. *Lithos* **2011**, *125*, 693–710. [[CrossRef](#)]

37. Xie, G.; Mao, J.; Zhu, Q.; Yao, L.; Li, Y.; Li, W.; Zhao, H. Geochemical Constraints on Cu–Fe and Fe Skarn Deposits in the Edong District, Middle–Lower Yangtze River Metallogenic Belt, China. *Ore Geol. Rev.* **2015**, *64*, 425–444. [[CrossRef](#)]
38. Craddock, P.R.; Rouxel, O.J.; Ball, L.A.; Bach, W. Sulfur Isotope Measurement of Sulfate and Sulfide by High-Resolution MC-ICP-MS. *Chem. Geol.* **2008**, *253*, 102–113. [[CrossRef](#)]
39. Ding, T.; Valkiers, S.; Kipphardt, H.; De Bièvre, P.; Taylor, P.D.P.; Gonfiantini, R.; Krouse, R. Calibrated Sulfur Isotope Abundance Ratios of Three IAEA Sulfur Isotope Reference Materials and V-CDT with a Reassessment of the Atomic Weight of Sulfur. *Geochim. Cosmochim. Acta* **2001**, *65*, 2433–2437. [[CrossRef](#)]
40. Xu, L.; Xie, Q.; Zhou, Y.; Wang, J.; Chen, T.; Xu, X.; Xie, J. Recognizing the Evolution of the Stratabound Polymetallic Massive Sulfide Deposits in Tongling Mineralization Cluster, East China through Colloform Pyrite. *Ore Geol. Rev.* **2022**, *146*, 104915. [[CrossRef](#)]
41. Ohmoto, H. Sulfur and Carbon Isotopes. In *Geochemistry of Hydrothermal Ore Deposits*; Wiley: Hoboken, NJ, USA, 1997; pp. 517–611.
42. Ohmoto, H. Systematics of Sulfur and Carbon Isotopes in Hydrothermal Ore Deposits. *Econ. Geol.* **1972**, *67*, 551–578. [[CrossRef](#)]
43. Seal, R.R. Sulfur Isotope Geochemistry of Sulfide Minerals. *Rev. Mineral. Geochem.* **2006**, *61*, 633–677. [[CrossRef](#)]
44. Anderson, G.M. Kerogen as a Source of Sulfur in MVT Deposits. *Econ. Geol.* **2015**, *110*, 837–840. [[CrossRef](#)]
45. Kesler, S.E.; Jones, H.D.; Furman, F.C.; Sassen, R.; Anderson, W.H.; Kyle, J.R. Role of Crude Oil in the Genesis of Mississippi Valley-Type Deposits: Evidence from the Cincinnati Arch. *Geology* **1994**, *22*, 609–612. [[CrossRef](#)]
46. Drummond, S.E.; Ohmoto, H. Chemical Evolution and Mineral Deposition in Boiling Hydrothermal Systems. *Econ. Geol.* **1985**, *80*, 126–147. [[CrossRef](#)]
47. Giggenbach, W.F. Geothermal Gas Equilibria. *Geochim. Cosmochim. Acta* **1980**, *44*, 2021–2032. [[CrossRef](#)]
48. Schaarschmidt, A.; Haase, K.M.; Klemm, R.; Keith, M.; Voudouris, P.C.; Alfieris, D.; Strauss, H.; Wiedenbeck, M. Boiling Effects on Trace Element and Sulfur Isotope Compositions of Sulfides in Shallow-Marine Hydrothermal Systems: Evidence from Milos Island, Greece. *Chem. Geol.* **2021**, *583*, 120457. [[CrossRef](#)]
49. Stefánsson, A.; Keller, N.S.; Robin, J.G.; Ono, S. Multiple Sulfur Isotope Systematics of Icelandic Geothermal Fluids and the Source and Reactions of Sulfur in Volcanic Geothermal Systems at Divergent Plate Boundaries. *Geochim. Cosmochim. Acta* **2015**, *165*, 307–323. [[CrossRef](#)]
50. Pan, Y.; Dong, P. The Lower Changjiang (Yangzi/Yangtze River) Metallogenic Belt, East Central China: Intrusion- and Wall Rock-Hosted Cu–Fe–Au, Mo, Zn, Pb, Ag Deposits. *Ore Geol. Rev.* **1999**, *15*, 177–242. [[CrossRef](#)]
51. Xu, X.C.; Yin, T.; Lou, J.W.; Lu, S.M.; Xie, Q.Q.; Chu, P.L. Origin of Dongguashan Stratabound Cu–Au Skarn Deposit in Tongling: Restraints of Sulfur Isotope. *Acta Petrol. Sin.* **2010**, *26*, 2739–2750. (In Chinese)
52. Zhou, T. Isotope Geochemistry of Copper Mineralization in Yueshan, Anhui. *Miner. Depos.* **1996**, *15*, 341–350.
53. Hu, D.L.; Jiang, S.Y.; Duan, D.F.; Xiong, S.F. Fluid Origin and Evolution of the Ruanjiawan W–Cu–(Mo) Deposit from the Edong District in the Middle–Lower Yangtze River Metallogenic Belt of China: Constraints from Fluid Inclusions and H–O–C–S Isotopes. *Ore Geol. Rev.* **2021**, *139*, 104428. [[CrossRef](#)]
54. Yan, D.R.; Deng, X.D.; Hu, H.; Li, J.W. U–Pb Age and Petrogenesis of the Ruanjiawan Granodiorite Pluton and Xiniushan Granodiorite Porphyry, Southeast Hubei Province: Implications for Cu–Mo Mineralization. *Acta Petrol. Sin.* **2012**, *28*, 3373–3388.
55. Deng, X.D.; Li, J.W.; Zhou, M.F.; Zhao, X.F.; Yan, D.R. In-Situ LA-ICPMS Trace Elements and U–Pb Analysis of Titanite from the Mesozoic Ruanjiawan W–Cu–Mo Skarn Deposit, Daye District, China. *Ore Geol. Rev.* **2015**, *65*, 990–1004. [[CrossRef](#)]
56. Chang, Z.; Meinert, L.D. The Empire Cu–Zn Mine, Idaho: Exploration Implications of Unusual Skarn Features Related to High Fluorine Activity. *Econ. Geol.* **2008**, *103*, 909–938. [[CrossRef](#)]
57. Chang, Z.; Meinert, L.D. The Magmatic–Hydrothermal Transition—Evidence from Quartz Phenocryst Textures and Endoskarn Abundance in Cu–Zn Skarns at the Empire Mine, Idaho, USA. *Chem. Geol.* **2004**, *210*, 149–171. [[CrossRef](#)]
58. Guilbert, J.M.; Park, C.F. *The Geology of Ore Deposits*, 4th ed.; WH Freeman: New York, NY, USA, 1986; p. 59.
59. Einaudi, M.T.; Hedenquist, J.W.; Inan, E.E. Sulfidation state of fluids in active and extinct hydrothermal systems: Transitions from porphyry to epithermal environments. In *Volcanic, Geothermal, and Ore-Forming Fluids: Rulers and Witnesses of Processes within the Earth*; Society of Economic Geologists, Special Publication: Littleton, CO, USA, 2003; pp. 285–314.
60. Sillitoe, R.H. Porphyry copper systems. *Econ. Geol.* **2010**, *105*, 3–41. [[CrossRef](#)]
61. Catchpole, H.; Kouzmanov, K.; Putlitz, B.; Seo, J.H.; Fontboté, L. Zoned base metal mineralization in a porphyry system: Origin and evolution of mineralizing fluids in the Morococha district, Peru. *Econ. Geol.* **2015**, *110*, 39–71. [[CrossRef](#)]
62. Zhai, D.G.; Williams-Jones, A.E.; Liu, J.J.; Selby, D.; Voudouris, P.C.; Tombros, S.; Li, K.; Li, P.L.; Sun, H.J. The genesis of the giant Shuangjianzishan epithermal Ag–Pb–Zn deposit, Inner Mongolia, Northeastern China. *Econ. Geol.* **2020**, *114*, 101–128. [[CrossRef](#)]

**Disclaimer/Publisher’s Note:** The statements, opinions and data contained in all publications are solely those of the individual author(s) and contributor(s) and not of MDPI and/or the editor(s). MDPI and/or the editor(s) disclaim responsibility for any injury to people or property resulting from any ideas, methods, instructions or products referred to in the content.